Computational Materials Science 197 (2021) 110618

Contents lists available at ScienceDirect

Computational Materials Science

journal homepage: www.elsevier.com/locate/commatsci

Compositional effects on stacking fault energies in Ni-based alloys using first-principles and atomistic simulations

Liubin Xu, Luis Casillas-Trujillo [1], Yanfei Gao, Haixuan Xu [*]

Department of Materials Science & Engineering and Joint Institute for Advanced Materials, The University of Tennessee, Knoxville, TN 37996, USA

ARTICLE INFO

Keywords:
Stacking fault energy
Twinning
Concentrated alloys
Density functional theory
Interatomic potential

ABSTRACT

Stacking fault energy (SFE) in fcc materials is a fundamental property that is closely related to Shockley partial dislocations and deformation twinning, the latter of which is potentially responsible for some of the exceptional mechanical properties observed in Ni-based high/medium-entropy alloys. In this study, the SFEs and twinning energies over a wide range of compositions are systematically determined in model Ni-based binary alloys using both first-principles density functional theory (DFT) and atomistic simulations with interatomic potentials. Particularly, different compositional dependences of SFEs are observed in the selected binary alloys (Ni-Cu, Ni-Co, and Ni-Fe) from DFT calculations. We find that SFEs of Ni-Co follow a linear-mixing rule while Ni-Cu and Ni-Fe systems exhibit non-linear compositional dependences, especially in the concentrated region towards the center of the phase diagram. Analyses of the magnetic structures help clarify the origins of the non-linear dependences. The fidelity of existing interatomic potentials for these alloys is evaluated against DFT. Using the interatomic potentials with the overall highest fidelity, the SFE calculations are extended to Cantor-related ternary alloys (Ni-Co-Cr and Ni-Co-Fe) and the spatial features of the fault energies in atomistic simulations are also discussed. These results provide the basis for a systematic understanding of the compositional effects on the SFEs and twinning energies, which could be useful for a systematic tuning of mechanical properties in non-equimolar alloys, thus leading to a broad field in alloy design.

1. Introduction

High entropy alloys (HEAs), or complex concentrated alloys (CCAs), or multiple principal elements alloys (MPEAs), have attracted tremendous research attention in the past decade [1–9]. In these alloys, there are multiple chemical species that have equal or similar concentrations, which is different from the conventional dilute-limit alloys. Some of the HEAs exhibit superior or even unprecedented mechanical properties [3–9]. For instance, it has been observed that both the ductility and the strength are increased when the temperature is decreased in the equiatomic face-centered cubic (fcc) CoCrFeMnNi (Cantor) alloy [10]. This is a desired but rare phenomenon, the underlying mechanism of which is not fully understood. Later, the same phenomenon was also observed in the subsets of the Cantor alloy, e.g., the equiatomic quaternary NiCoCrFe, ternary NiCoFe and NiCoCr, and binary NiFe and NiCo alloys [11].

To understand the physical origin of the observed mechanical behavior, we must investigate the underlying deformation mechanisms. For fcc metals and alloys, their yield strength is generally linked with the glide of the $1/6\langle 1\,1\,2\rangle$ Shockley partials, which originates from the disassociation of a perfect dislocation ($1/2\langle 1\,1\,0\rangle$) and is connected by a stacking fault region. Meanwhile, the ultimate strength and ductility often involve the interplay between faulted structures (stacking faults and deformation twinning), dislocations, and grain boundaries. Specifically, in the Cantor alloy and its subsets, the deformation twinning is observed at the low temperature (77 K) [10,11] and is postulated to be responsible for the simultaneous increase in both strength and ductility. For example, it can serve as an obstacle that hinders dislocation motion and therefore increase the strength of materials [12,13]. Meanwhile, the deformation twinning has also been implied to contribute to work hardening and delay the necking instability via dynamic Hall-Petch effect [10,11,14]. Therefore, determining the energetics and stabilities of stacking faults and twins is essential for a fundamental understanding of the deformation processes of these alloys.

Generally speaking, experimental values of the stacking fault energy (SFE) in alloys can be determined from the width of separation between

* Corresponding author.
E-mail address: xhx@utk.edu (H. Xu).
[1] Current address: Department of Physics, Chemistry and Biology (IFM), Linköping University, SE-581 83 Linköping, Sweden.

https://doi.org/10.1016/j.commatsci.2021.110618
Received 19 January 2021; Received in revised form 20 April 2021; Accepted 27 May 2021
Available online 16 June 2021

a pair of Shockley partials measured by Transmission Electron Microscopy (TEM) [15–17] or from the stacking fault probability using the X-ray diffraction line broadening [18]. For instance, the SFE of the Cantor alloy was measured to be 25–35 mJ/m^2 from the TEM experiments [15] and 18–27 mJ/m^2 using the X-ray technique [18]. Qualitatively, the two values agree well as both indicate the Cantor alloy belongs to low SFE materials. Quantitatively, the ~10 mJ/m^2 difference between the studies might come from their different thermal treatments of the samples and specific approximations used to convert the measured quantities to SFEs. Additionally, the disassociation width of a pair of Shockley partials in concentrated alloys can vary spatially by a factor of 1.5 even in an individual study throughout which the thermal treatments and the approximations are consistent [15–17]. This implies the existence of spatial fluctuation of the SFEs, which can be a distinct source of strengthening as suggested by recent theoretical studies [19,20].

Theoretical investigations of the SFEs for the Cantor and related alloys have been carried out using density functional theory (DFT) in the past years [21–31]. Many of these investigations focused on an accurate determination of the SFE at a single, usually the equiatomic, composition, for which the importance of temperature [21,22] and magnetism [23] has been demonstrated. A few studies examined the dilute-limit alloying effects on SFEs by either substituting with other metallic elements [24,25] or adding carbon [26]. The SFEs at small scales have been found to be sensitive to the local chemical order (short-range order) and exhibit strong fluctuation [23,27,28]. For instance, Zhao *et al.* [28] have examined the influence of local composition on the SFEs with equiatomic composition and proposed a bond-breaking- and-forming model. Nevertheless, the model is not sufficiently accurate for either NiFe or NiCoCr despite its success in NiCo alloy. Moreover, DFT-based Monte Carlo studies suggested that the local chemical order influences not only the spatial distribution of SFEs but also the mean value [29,30] which is verified recently in experiments [32]. Additionally, the coherent-potential-approximation (CPA) has been used to calculate the compositional dependence of SFEs [27,31]. However, the effects of atomistic distortion on the SFEs cannot be included by the CPA, and the distortion can be substantial in HEAs.

Atomistic simulations also provide a powerful means to study mechanical properties of metals and alloys. Compared with DFT, atomistic approach can sample more configurations and larger system sizes and can be directly used to simulate deformation processes (e.g. [33]). Nevertheless, the chemical complexity of HEAs poses a considerable challenge to the development of reliable interatomic potentials. Only a few reasonable interatomic potentials became available recently for the Cantor and Cantor-like alloys [33,34]. Therefore, it is essential to understand the fidelity and limitations of these potentials. SFEs influence many aspects of mechanical properties and deformation behaviors of these alloys, and the values from these interatomic potentials should be carefully assessed.

Overall, tuning the compositions of constituent elements away from the equiatomic HEA/MEAs offers a vast playground for controlling mechanical properties of materials. However, a systematic understanding of compositional effects on the SFEs, especially the role of the constituent elements, is currently limited. In this study, we systematically investigate the compositional effects on SFEs in the binary (Ni-Cu, Ni-Co, and Ni-Fe) and ternary (Ni-Co-Cr and Ni-Co-Fe) alloys using both DFT and interatomic potentials. We first calculate the SFEs and the corresponding fluctuations at the DFT level as a function of composition in the binary alloys, with an emphasis on examining the magnetic/electronic effects of an individual alloying element. Then atomistic calculations using interatomic potentials are evaluated against the DFT data. We further choose the interatomic potentials with the overall highest fidelity and extend the SFE calculations to ternary alloys.

2. Computational method

2.1. Stacking fault energy calculation

SFE is determined by subtracting the energy of a stacking fault structure from that of its un-faulted reference structure. The reference fcc supercell can be viewed as the stacking of (1 1 1) closed-pack layers in alternating ABC sequence along [1 1 1] axis (Fig. 1a). To introduce a stacking fault in the structure, we arbitrarily choose a layer in the reference structure, e.g., the 7th layer from the bottom, displace the atoms of above (not including) this layer by $\frac{1}{6}\left[\bar{2}11\right]$, and tilt the supercell by $\frac{1}{6}\left[\bar{2}11\right]$ in the z-axis. The tilting helps to prevent an unfavorable AA-type stacking at the supercell boundary. The product of the above deformation process, illustrated in Fig. 1b, is an intrinsic stacking fault (ISF) with two layers, 7th and 8th, of ABA-type local stacking. Due to the tilting, the 13th layer in the above supercell, which is the periodic image of the 1st layer, is changed from A stacking type to B, but its local environment remains unchanged. The SFE is then the energy difference between the structures in Fig. 1a and b divided by the area of the (1 1 1) plane.

This procedure can be naturally extended to calculate the generalized planar fault energies (GPFEs)/generalized stacking fault energies (GSFEs) [35,36]. For example, based on the ISF structure in Fig. 1b, we could add another displacement of $\frac{1}{6}\left[\bar{2}11\right]$ to the atoms above (not including) 8th layer and tilt the supercell one more time by $\frac{1}{6}\left[\bar{2}11\right]$ to obtain a twinning (Fig. 1c). If we select the atoms one layer higher each time and repeat this process, the twin would grow into an generalized planar fault with a gradual increase of the fault layer thickness, namely the three-layer twin, four-layer twin, etc. The energy difference between the fault structure and the reference structure divided by twice of the fault area, is defined as the corresponding GPFE/GSFE. Note that the coefficient of 2 in the denominator, except for the calculation of SFE, comes from the presence of two coherent twin boundaries (CTBs) in the fault structures, e.g., 7th and 8th layer in Fig. 1c.

The energies involved in the above procedure can be calculated using both DFT approach and interatomic potentials. Among the interatomic potentials, embedded-atom-method (EAM) type and its extension are widely chosen for simulations of metals and alloys. The DFT method is more accurate and provides an explicit description of magnetism when compared to the EAM potentials. However, the system size that can be dealt with DFT is rather limited, usually up to several hundred atoms. By contrast, EAM potentials allow the usage of much larger supercells and more random configurations to obtain the statistically accurate mean of SFE.

2.2. Density functional theory calculations

The DFT calculations for the SFEs of the binary alloys are carried out using the Vienna Ab initio Simulation Package (VASP) [37,38]. The Perdew-Burke-Ernzerhof (PBE) functional [39] is used. The energy cutoff of the plane wave basis is tested and chosen to be 450 eV, 450 eV, and 500 eV for Ni-Cu, Ni-Co, and Ni-Fe, respectively. (Here, the hyphen indicates a range of compositions, e.g., Ni-Cu for Ni_xCu_{1-x}. In comparison, alloy notation without a hyphen means the equiatomic composition, e.g., NiCu for $Ni_{0.5}Cu_{0.5}$). Since an energy difference is taken for each of the investigated systems, these different choices of energy cutoff will not influence the conclusions drawn in the paper. The first order Methfessel-Paxton [40] method is used with the smearing width set as 0.2 eV. The electronic convergence criterion is set as 10^{-6} eV and the ionic force criterion is 0.01 eV/Å. All the calculations are spin-polarized unless explicitly mentioned otherwise. The initial magnetic

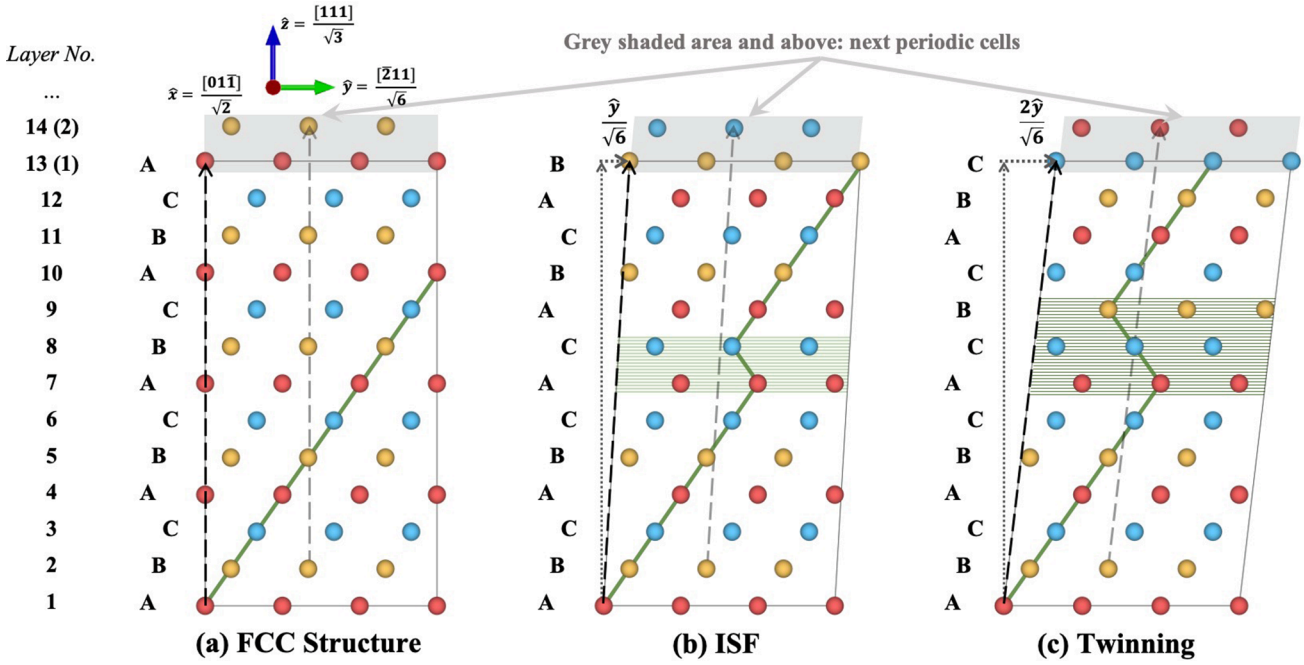

Fig. 1. Atomistic illustration of (a) a perfect fcc lattice, (b) an intrinsic stacking fault, and (c) a two-layer twinning structure. The grey shaded areas indicate the next periodic cells. The light green in (b) and the dark green in (c) demonstrate the ISF and the twinning regions, respectively.

configurations are set as ferromagnetic, which agrees with previous studies [41,42] at low temperatures. To improve the statistical sampling of the random solid solutions, we utilize special quasirandom structures (SQSs) [43] generated by the Alloy Theoretic Automated Toolkit (ATAT) [44,45]. Using the SQS method implies that short-range ordering (SRO) is not explicitly considered for the mean value of SFE, which should be a reasonable assumption for binary alloys where SRO should be minimal.

We first carry out structural optimization and determine the lattice constants (a_0) of the selected alloys in wide compositional ranges with $2 \times 2 \times 2$cubic SQS supercells consisting of 32 atoms. For each composition, three different SQSs are used and the average value is obtained. We then use a spline fit to derive the lattice constants across the whole compositional range for each of the alloys. For the $2 \times 2 \times 2$ cubic supercells, a $4 \times 4 \times 4$ k-point mesh of Monkhorst-Pack [46] grid is used. With the determined lattice constants, SFE calculations are performed with $\sqrt{2} \times \sqrt{6} \times 4\sqrt{3}$ (using the same coordinate system as shown in Fig. 1a, referred as the close-packed axes) SQS supercells of 96 atoms. Every 8.33% of nickel atomic concentration (all concentrations mentioned below are atomic percentages) is tested across the whole compositional range, and six different SQSs are generated at each concentration. For each SQS, we choose four different layers, every two-layers apart from each other, to introduce a stacking fault in both $\frac{1}{6}\left[\bar{2}11\right]$ and $\frac{1}{6}\left[2\bar{1}\bar{1}\right]$ directions. Consequently, 48 different faulted configurations are utilized for the average of the SFE at a single composition. For the $\sqrt{2} \times \sqrt{6} \times 4\sqrt{3}$ supercell, a $6 \times 4 \times 2$ k-point mesh is used. The combined energy-cutoff, k-point, and smearing settings ensure the energetic accuracy of 1 meV/atom, leading to the error of around 12 mJ/m^2 for the SFE of a single SQS. The error for the mean value of SFE is further reduced to $\frac{12}{\sqrt{48}} \approx 2$ mJ/m^2.

2.3. Atomistic simulations with EAM potentials

For the binary alloys, we survey all the relevant EAM potentials listed on the interatomic potential repository from the National Institute of Standards and Technology (NIST) [47]. For convenience, we refer each EAM potential by the last name of the first author plus the publication year. Bonny2009 [48] Farkas2018 [34] and Onat2013 [49] potentials are tested for Ni-Cu alloy; Farkas2018 [34] and PurjaPun2015 [50] for Ni-Co alloy; Bonny2009 [48] Bonny2011 [51] Bonny2013 [52] Farkas2018 [34] and Zhou2018 [53] for Ni-Fe alloy. In addition, a modified EAM (MEAM) potential, Choi2018 [33] is also used for Ni-Co and Ni-Fe alloys. For the ternary alloys, Farkas2018 [34] and Choi2018 [33] are used (the reason to be discussed in the Results & Discussion section).

The simulations are performed in Large-scale Atomic/Molecular Massively Parallel Simulator (LAMMPS) [54]. Similar to the DFT part, lattice parameters are first obtained for every 10% Ni concentration for each alloy. At each concentration, 10 random atomic configurations of $40 \times 40 \times 40$(in cubic axes) are generated and optimized in both atomic positions and cell volumes. The standard deviations (Std Dev) of the obtained lattice constants are less than 10–4 Å, and averaged lattice constants are used in later calculations. For the SFE calculations, another 40 random configurations of size $16\sqrt{2} \times 16\sqrt{6} \times 16\sqrt{3}$ (in close-packed axes) are utilized. Both the Std Dev and the standard error (Std Err) of SFE are reduced when the area of the faulted plane is increased (see Fig. 2a and 2b). In comparison, the number of random configurations used for averaging only reduces the Std Err, but not the Std Dev (Fig. 2c and 2d). Accordingly, the supercell size and the number of random configurations are chosen so that the Std Err of SFE at any concentration is around 1 mJ/m^2.

2.4. Correlation between SFEs and TEs

The twice TE is often assumed to be approximately equal to the SFE of the same system and this assumption has been verified in many pure fcc metals both experimentally and computationally using DFT calculations (e.g., Table 1 in [35]). We further examine this approximation in the selected binary alloys using various interatomic potentials and find that the approximation holds in the alloys as well (shown in Fig. 3a). The numerical differences between the SFEs and twice TEs are always less than 5%, and their overall compositional dependences are the same.

To elucidate the correlation between SFEs and TEs, we first define the "atomic fault energy" (AFE), which is the product of the planar atomic density of {1 1 1} layers and the energy difference per atom before and after the faulted structure is generated. Next, we take the

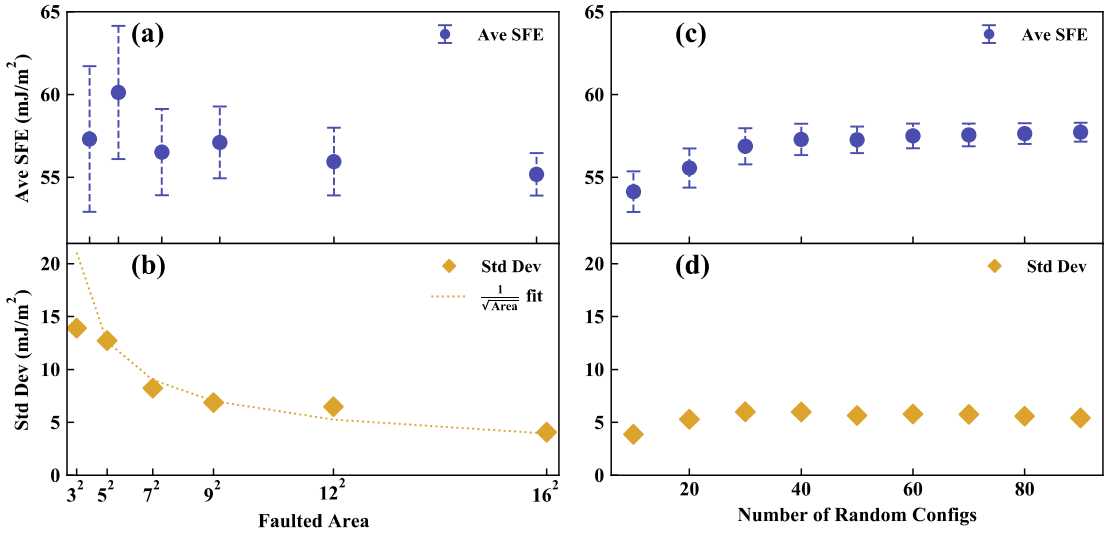

Fig. 2. (a) The obtained average SFE and (b) the Std Dev as a function of supercell size; (c) the obtained average SFE and (d) the Std Dev as a function of the number of random configurations for Ni0.5Fe0.5 using the Farkas2018 potential. The faulted area is $\frac{\sqrt{2}}{2}N \times \frac{\sqrt{6}}{2}N$, $N = 3, 5\ldots,16$, in unit of a02. For (a) and (b) (left column), 10 random configurations are used in the calculation while in (b) and (d) (right) the faulted area are kept at 16 × 16.

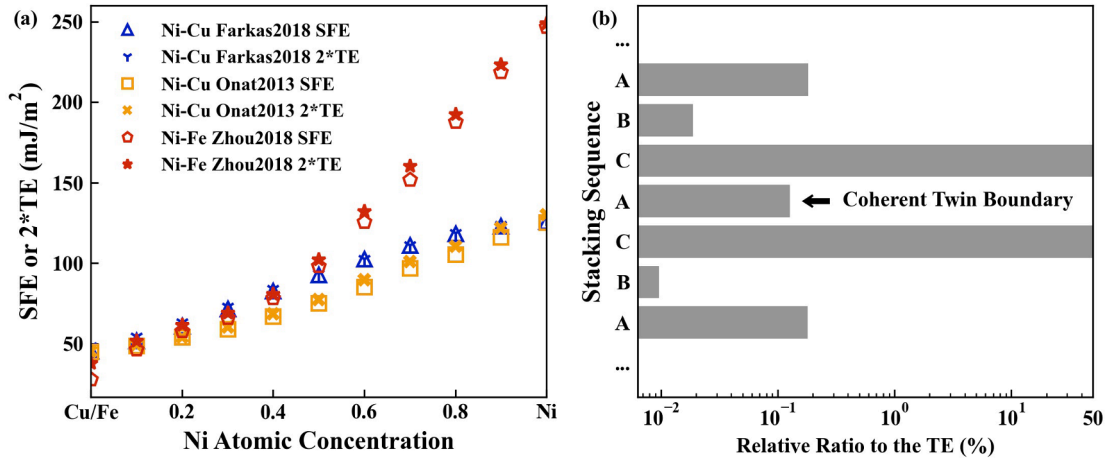

Fig. 3. (a) SFEs and TEs as a function of Ni composition using various interatomic potentials and (b) relative layer contributions (absolute value) of the parallel (1 1 1) planes to the total TE in log-scale.

average AFE of a {1 1 1} plane that is parallel to the CTB (in Fig. 1's case, a (1 1 1) plane) as the fault energy of that layer, referred as the layer's contribution to the total planar fault energy. We then calculate the contribution from each layer to the TE of a large twinning structure (~30 nm^2) at composition $Ni_{0.5}Fe_{0.5}$ using the Farkas2018 potential as an example. The twin is created through the repeat of the aforementioned process till the two CTBs are well separated (~7.3 nm in our case). Absolute values of the layer contributions relative to the total TE around a CTB (layer A in the middle) is plotted in Fig. 3b. Each of the two nearest (1 1 1) layers to the CTB, namely the C layers, contributes ~50% to the TE. For a C-layer, the energy difference comes from the change in 2nd nearest layer interaction, e.g., from **C**-*A*-**B** to **C**-*A*-**C**, while its 1st nearest layer interaction remains more or less the same. The rest layers contribute statistically zero to the TE. Therefore, we can conclude that the dominant part of fault energies, whether SFE or TE, can be estimated based on the 2nd nearest layer changes from **C**-*A*-**B** type to **C**-*A*-**C**. A stacking fault contains two pairs of such changes (e.g., 6th − 8th and 7th − 9th in Fig. 1b) while the TE is calculated based on one such change. Based on this argument, we consider the approximation that the twice TE is equal to the SFE is reasonable, and hence focus only on the SFE for the rest of the study. The approximation can be also reasoned, for example, using the axial-next-nearest-neighbor-interaction model [55].

3. Result and discussion

3.1. Binary alloys

3.1.1. Lattice constants

The lattice parameters of Ni-X (X = Cu, Co, or Fe) alloys obtained from DFT and EAM potentials are shown in Fig. 4, compared with the experimental values. Both Ni-Cu and Ni-Co experimentally obey Vegard's law [59], an empirical rule stating that the lattice constant of an alloy should be approximately the linear mixing of those of the constituent elements in the same crystal phase. In comparison, Ni-Fe alloys experimentally exhibit a linear increase as the Ni concentration decreases from 100% to 35%, and then a decrease when Ni is further reduced. This is attributed to the Invar effect, the underlying physical origin of which is closely related to magnetism [60,61]. Our DFT-SQS results of the 3 binary alloys all agree well with the experiments regarding the numerical values and the general trends, e.g., obeying the Vegard's law at relevant compositions as well as qualitatively capturing the Invar in Ni-Fe. Nevertheless, we notice two differences between the

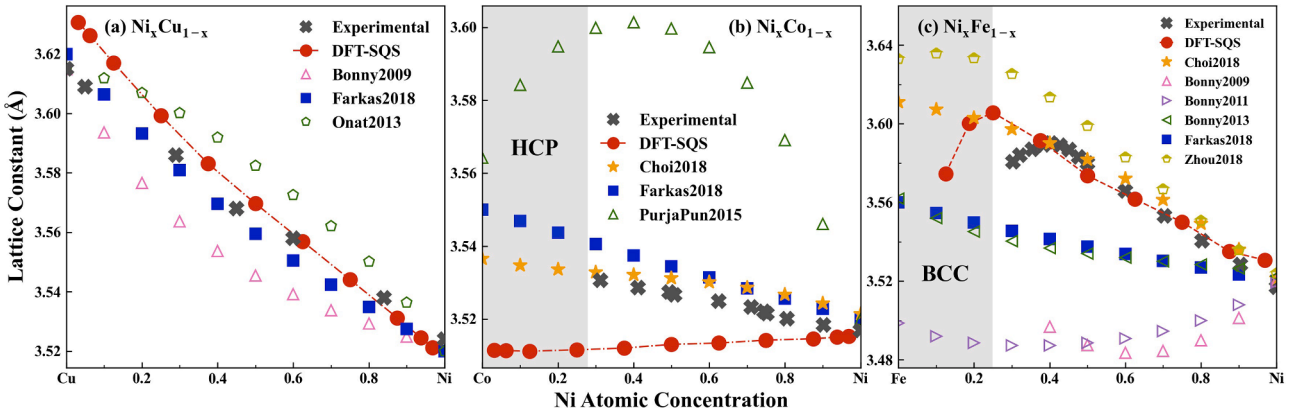

Fig. 4. Lattice constants of (a) Ni-Cu, (b) Ni-Co, and (c) Ni-Fe binary alloy. The experimental values of fcc Ni-Cu, Ni-Co, and Ni-Fe are from references [56], [57], and [58], respectively, and the measurements are performed at 300 K. Non-fcc phase in the experiments are shaded and lines are added to guide the eye.

DFT results and the experiments. First, the DFT calculation for Ni-Co predicts an increasing trend of the lattice constant with increasing Ni concentration, while the experimental trend is decreasing. We consider this difference comes from the fact that our simulation yields a lattice constant of 3.505 Å for the fcc Co, which is smaller than that of Ni (3.521 Å). Experimentally, Co prefers hexagonal close-pack (hcp) structure for the room or lower temperatures at ambient pressure. We did not find any experimental lattice parameter of fcc Co at low temperatures that can be used as a direct reference for the DFT calculation. However, it should be noted that the differences between the experimental and our calculated lattice parameters of Ni-Co are less than 1%, reaching the accuracy limit of standard DFT simulations. Some of previous studies observed equal or slightly smaller values of fcc Co lattice constant than Ni's using local spin density approximation [62,63]; while another study obtained Co lattice constant larger than that of Ni using PBE functional but with exact-muffin-tin-orbital (EMTO) method [64]. Second, in the Ni-Fe, the Ni composition of the maximum lattice constant using DFT (~25%) does not agree with that from the experiment (35%). This is because high-spin/low-spin model and non-collinear magnetism needs to be included to accurately model Invar effects [60,61] which is not included in our simulations due to computational costs. Therefore, we only focus on the concentrations above ~40% for the following SFE calculations in Ni-Fe.

We also examine the lattice constants among the three SQSs of a particular concentration and find their differences are always smaller than 0.001 Å. This suggests that the lattice constant is not sensitive to the atomic configuration used in the DFT simulation but solely determined by the overall composition, which is in dramatic contrast to the case of SFE calculation (to be discussed in Section 3.1.2).

Regarding the lattice constants from the interatomic potentials, we assess them in terms of the numerical value and the observance of Vegard's law. For Ni-Cu, Farkas2018 agrees well with the experiments and reproduces the linear relationship. Bonny2009 and Onat2013 deviate more from the experimental values, although they also generally follow the Vegard's law. For Ni-Co, both Farkas2018 and Choi2018 display excellent agreement with the experiments. PurjaPun2015 exhibits an unreasonable trend. For Ni-Fe, Choi2018 reproduces the experimental and DFT data well. Bonny2013, Farkas2018, and Zhou2018 follow the linear-mixing rule approximately, but their numerical values are not as accurate as the Choi2018's. Bonny2009 and Bonny2011 fail to capture the linear mixing of lattice constants in high Ni-concentrations. To summarize the potentials' performance, we consider that MEAM Choi2018 and EAM Farkas2018 provide the overall best description of the lattice constants based on the numerical agreement and the linear compositional dependence.

3.1.2. Stacking fault energies

The SFEs of the three binary alloys are shown in Fig. 5. We find that the SFEs of Ni-Cu exhibit a complex dependence on the composition (Fig. 5a). When the Ni concentration is low, the SFEs rise rapidly and reach a plateau around $Ni_{0.4}Cu_{0.6}$; when Ni percentage exceeds about 50%, the SFE increases approximately linearly with the Ni composition. We refer this as the transition of SFE dependence. We then compare the SFEs from the interatomic potentials with the DFT results. The numerical values obtained with Farkas2018 and Onat2013 are close to those from DFT. The SFE dependence from neither potential is far from linear mixing. Farkas2018 shows a slightly convex dependence while Onat2013 exhibits a slightly concave trend. In contrast, Bonny2009 exhibits a substantial discrepancy from the other curves. None of the interatomic potentials reproduces the subtle variation of the SFEs around $Ni_{0.4}Cu_{0.6}$ shown in the DFT simulations.

The SFEs of Ni-Co are shown in Fig. 5b. The SFEs from DFT display an overall linear dependence as a function of composition. However, their values are negative in the Co-abundant region (Ni percentage less than 50%), suggesting the hcp phase is more stable than the fcc phase. This is qualitatively consistent with Ni-Co phase diagram [57]. The overall linear dependence is consistent with the study of local compositional effects in the equiatomic NiCo [28]. For the calculations using the interatomic potentials, the SFEs from Choi2018 and Farkas2018 agree reasonably well with the DFT results. Nevertheless, both potentials yield higher SFEs than DFT in the Co-abundant region. PurjaPun2015 produces extremely higher SFEs in the concentrated region than those from DFT. Together with its performance on the lattice constant, we consider that the PurjaPun2015 is not suitable for model fcc Ni-Co concentrated alloys.

Fig. 5c shows the SFEs of Ni-Fe. The DFT values exhibit a unique non-monotonous and concave compositional dependence. The SFE decreases first when the iron is started to be alloyed to pure Ni but then increases when iron concentration continues to grow above 25%. None of the interatomic potentials captures this trend from DFT. All the potentials, except Bonny2009, display a linear decrease when the Ni concentration is reduced. Choi2018 and Bonny2013 exhibit slopes that are almost indistinguishable from the DFT's in the dilute-Fe region but miss the value of equiatomic NiFe. Comparatively, Bonny2011 and Farkas2018 coincidentally show SFE values of NiFe (and the concentrated region) that are close to the DFT's, despite the disagreement with DFT regarding the initial slope near pure Ni. Zhou2018 overestimates the SFE of Ni though it provides a good approximation for the SFE of NiFe. Bonny2009 underestimates the SFE of Ni and exhibits a convex dependence, quite the opposite to the compositional dependence from DFT.

To briefly summarize the SFE results of the binary alloys, the DFT calculations reveal three distinctive compositional dependences of SFE in Ni-Cu, Ni-Co, and Ni-Fe alloys. The non-linear effects are speculated

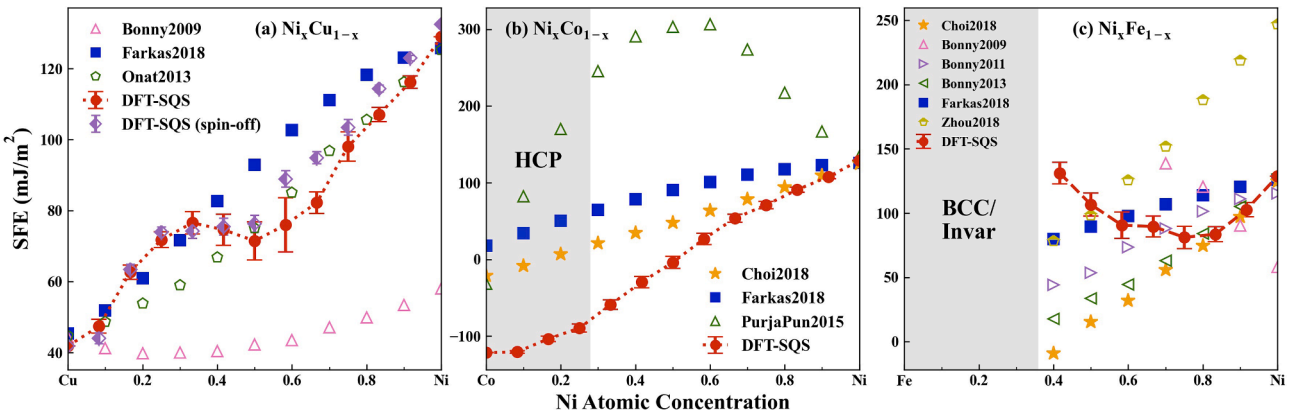

Fig. 5. Averaged intrinsic SFEs of (a) Ni-Cu, (b) Ni-Co, (c) Ni-Fe binary alloy as a function of Ni concentration. The standard errors of the SFEs from interatomic potentials are on the order of 1 mJ/m^2, a value too small to be seen in the figure.

to be related to the magnetic and electronic characters of the alloying elements and subsequently investigated in section 3.1.3. None of the interatomic potentials can capture these subtle effects. Choi2018 and Farkas2018, though being the only two potentials that can model alloys with 4 or more elements up to date and are the harder ones to fit, display overall the best performance in terms of numerical accuracy and consistency of capturing linear mixing over a wide range of compositions. We choose these two potentials for the subsequent SFE calculations of the ternary alloys.

3.1.3. *Magnetic effects on the SFEs in the binary alloys*

To reveal the underlying origin of the non-linear SFE dependences, we further analyze the magnetic and electronic structures of Ni-Cu and Ni-Fe. For Ni-Cu (Fig. 6a), the transition of the SFE dependence coincides roughly with the magnetic phase transition from paramagnetism to ferromagnetism in the alloy. Therefore, we speculated that the transition of the SFE dependence is closely linked to the magnetism of Ni-Cu. To examine this, we artificially turn off the spin degree of freedom in the DFT calculations. The spin-unresolved results exhibit the transition of the SFE dependence as well. In the Cu-rich region, the two methods yield essentially identical results (within the statistical error). However, in the Ni-rich region, SFEs using the spin-unresolved calculations are systematically higher than the spin-resolved results. Therefore, we consider that the non-linear dependence in the Cu-rich region has its root in the electronic effects, potentially due to the screening of the d-orbitals in Cu. In comparison, the magnetism reduces the SFEs in the Ni-rich region by about 10 mJ/m^2.

For Ni-Fe alloys, we find a correlation of the SFEs and the magnetic moment differences between the faulted and the reference structures, shown in Fig. 6b. In addition to the linear-mixing rule, the energy variation arising from the change in magnetic moments also contributes significantly to the compositional dependence of the SFEs. Thus, we fit the SFE as a linear function of both Ni concentration x and magnetic moment difference Δm:

$$SFE = a^*x + b^*\Delta m + SFE_0$$

and obtain the coefficient a equal to −64.1088 mJ/m^2, b 293.2951 mJ/m^2/μB, and SFE_0 142.3513 mJ/m^2 while the R-squared (the correlation coefficient-squared) is equal to 0.922. This strong correlation between the SFEs and x and Δm indicates that both the linear mixing and the magnetic moment difference are the dominating factors for the SFEs of Ni-Fe alloy.

3.1.4. *Statistical fluctuation of the SFEs from DFT*

The SFEs of the various atomistic configurations that belong to the same chemical composition are found to fluctuate tremendously, which is in stark contrast to the calculations of lattice constants. This fluctuation is also the reason that 48 configurations for each composition are used to achieve an acceptable Std Errs of the mean. In Fig. 7, we explicitly plotted the SFE of every configuration minus the average value of the corresponding concentration.

Std Devs are used to characterize the spread of the SFE data. The Std Devs are typically on the order of 20–40 mJ/m^2, which ranges from 15% to 30% of the mean SFEs at the equiatomic concentration. Std Devs of both Ni-Cu and Ni-Co alloys, shown in Fig. 7a and Fig. 7b, respectively, are peaked around the equiatomic region and diminish to 0 at pure

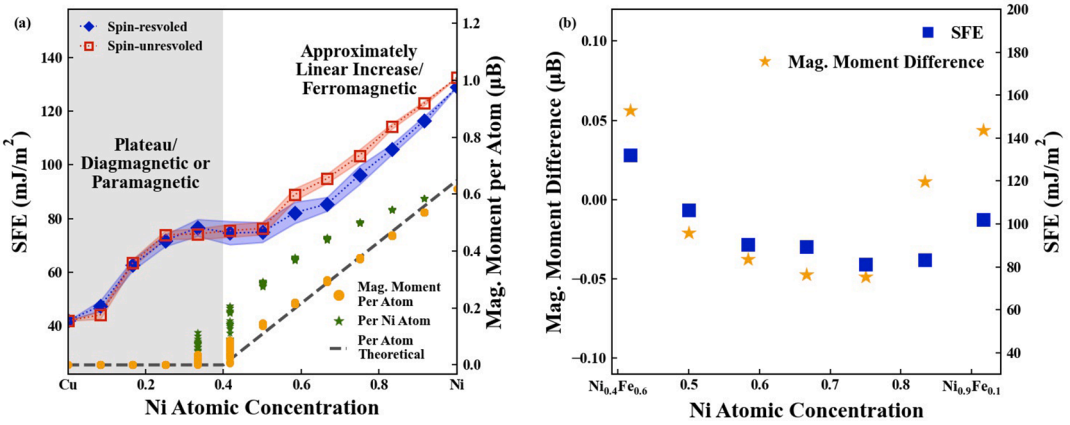

Fig. 6. Magnetic analysis in (a) Ni-Cu and (b) Ni-Fe alloy from DFT calculations. The theoretical values of Ni-Cu magnetic moments are taken from [41]. The colored bands are added to indicate the statistical range of the mean of the SFEs.

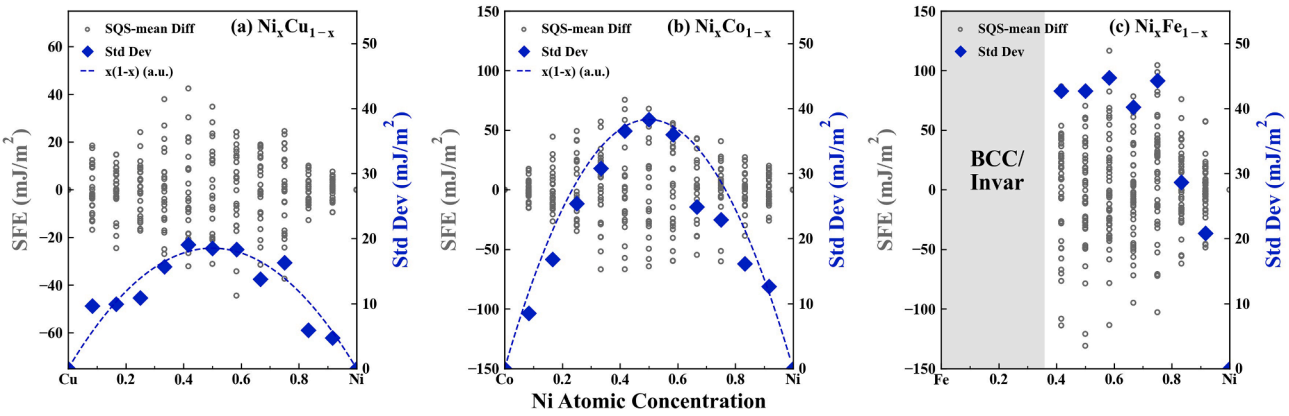

Fig. 7. The variations of SFEs from their mean value at every concentration in the three binary alloys. The right *y*-axis represents the Std Dev of the data.

metals. The relationship can be fitted by $A \times x \times (1-x)$, where A is a fitting coefficient and the x is the Ni percentage. The fitting agrees with the mixing entropy of the binary alloys regarding the overall trend, implying that the number of possible alloy configurations may be a key factor causing the fluctuations of the SFEs in the two alloys. However, in the Ni-Fe case, the Std Devs can't be well approximated by the above relationship and is comparatively higher than the other two alloys. This is considered to be related to the complex magnetism in Ni-Fe. A previous study [23] has found that the presence of Cr or Mn in the Cantor alloy and its subsets can induce larger fluctuations of SFEs than Co. However, such fluctuation is caused by magnetic frustration. The magnetic moment per atom of the same species can vary significantly (~1μB scale) at different lattice sites. However, in Ni-Fe, the magnetic moment the per atom differs less than 0.01 μB. Therefore, further investigation is needed to fully understand the role of Fe magnetism in the fluctuations of SFEs.

Nevertheless, the substantial fluctuation of certain materials properties, such as SFEs, can be a fundamental difference between

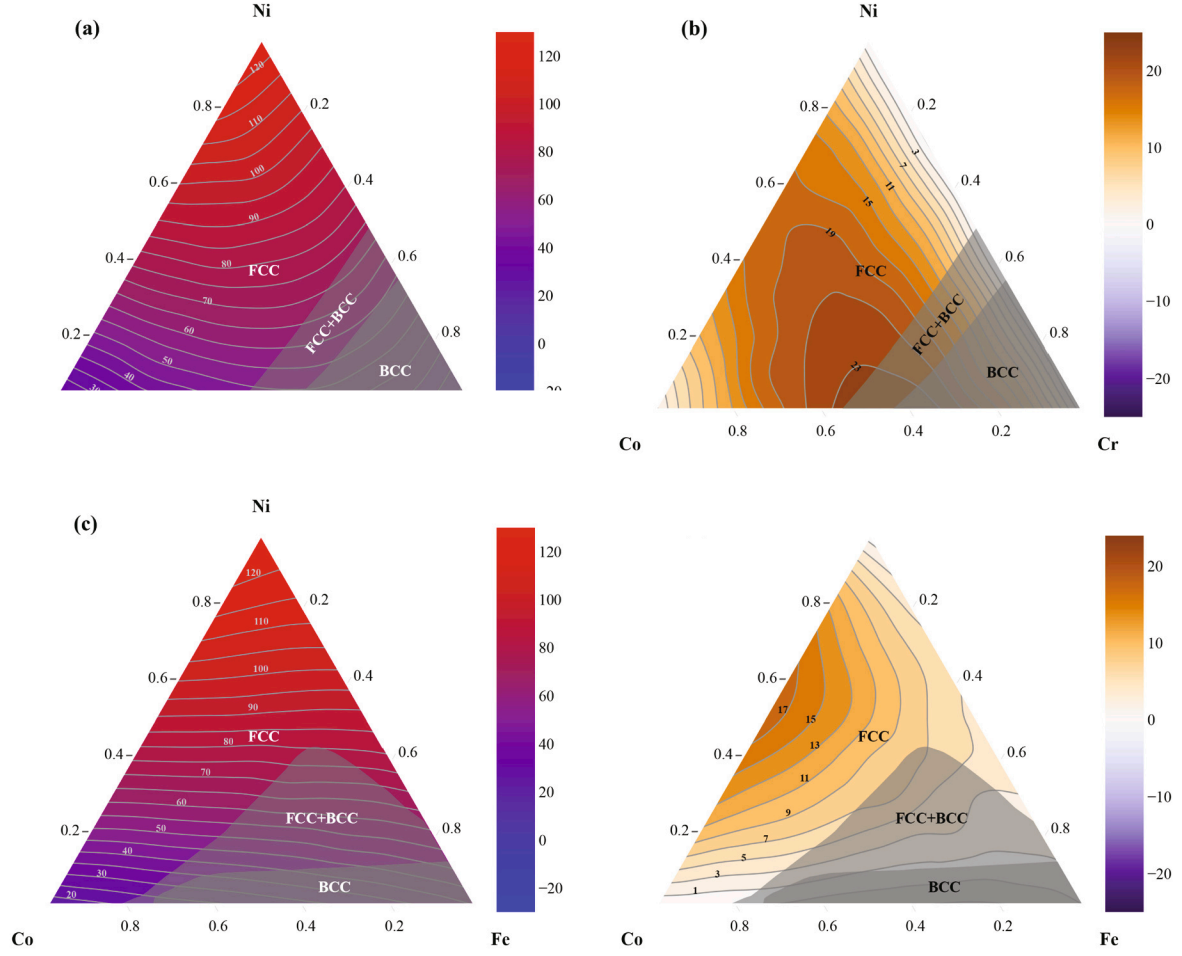

Fig. 8. Farkas2018 results of (a) the SFEs of Ni-Co-Cr ternary alloys, (b) their differences from the linear-mixing estimation, (c) the SFEs of Ni-Co-Fe alloys, and (d) their differences from the linear-mixing estimation. The phase information is obtained at 1300 °C for Ni-Co-Cr [65] and 600 °C for Ni-Co-Fe [66]. The contour lines are rendered in gray. The unit of the color bars is mJ/m^2.

concentrated and dilute alloys. We systematically quantify the magnitude of the fluctuation in the binary concentrated alloys and find the fluctuation of SFEs strongly depends on the composition. The fluctuation of SFEs is substantial in nanometer scale, for example, around 20–50 mJ/m^2 at 50% Ni in the three binaries. Such fluctuations may be practically difficult to observed in experiments, but could account for, at least partially, the exceptional strengths of the Cantor and Cantor-like alloys. It should be noted that such fluctuation is observed without SRO, and SRO may lead to additional variations of the SFEs [29,30,32].

3.2. SFEs of ternary alloys

The SFEs of Ni-Co-Cr and Ni-Co-Fe alloys, two ternary subsets of the Cantor alloy, are determined using Farkas2018 and Choi2018. Similar to the simulations of the binary alloys, the lattice parameters are pre-optimized. We found the lattice parameters of both alloys can be well approximated using the weighted average of those of the constituent elements, a simple extension of Vegard's law into alloys with three or more elements. The maximum difference between the values estimated from the linear-mixing rule and the optimized lattices is less than 0.003 Å.

The SFEs calculated using the Farkas2018 potential are shown in Fig. 8. In both Ni-Co-Cr and Ni-Co-Fe, SFEs obtained using Farkas2018 are larger than the values based on the linear mixing of the constituent elements' for most of the regions of the ternary diagram. In the Ni-Co-Cr case (Fig. 8a and 8b), the deviation of calculated SFEs from the linear mixing occurs mostly in the region when Co concentration is around 50% ($Ni_xCo_{0.5}Cr_{0.5-x}$). The non-linearity can be decomposed and attributed to the binary subsets (illustrated as the three edges of the ternary plots): the Ni-Cr obeys the linear mixing perfectly while the Ni-Co deviates by a small amount, and the Co-Cr deviates from it most significantly. Therefore, it is considered that the dominant contribution to the non-linear effects come from the Co-Cr pair interaction, followed by Ni-Co interaction. For the Ni-Co-Fe (Fig. 8c and 8d), the linear mixing provides a slightly better estimation than the previous case. The maximum difference occurs around $Ni_{0.5}Co_{0.5}$ and reduces to almost zero in both Ni-Fe and Co-Fe edges.

The SFE of equiatomic NiCoCr from Farkas2018 is 73.6 mJ/m^2, a value significantly larger than the experimental results of 8.18 ± 1.43 (without SRO) or 23.33 ± 4.31 (with SRO) [32]. This could be partially expected from its overestimation of the SFE of Co. The overestimation of the SFE suggests that simulations with the Farkas2018 potential are less likely to produce deformation twinning, particularly at low temperatures.

We also compare our results to the local compositional effect on the SFEs in the Ni-Co-Cr alloy obtained using CPA [27]. It should be noted that the composition was only changed at the layers with local hcp structure (corresponding to 7th and 8th layers in Fig. 1b) in the CPA study [27] while the other layers were kept at equiatomic NiCoCr composition. Therefore, the comparison is not strictly one-to-one but qualitative, as we have already demonstrated the importance of the next nearest neighbor layers in Section 2.4. Firstly, we find the relative magnitudes of the SFEs of the three constituent elements are the same in both studies ($SFE_{Ni} > SFE_{Cr} > SFE_{Co}$). Furthermore, the SFEs of the three binary subsets are examined and compared. For the Ni-Cr subset, Farkas2018 yields a linear dependence, while the SFEs from CPA decrease from Ni to $Ni_{0.5}Cr_{0.5}$ and increase from $Ni_{0.5}Cr_{0.5}$ to Cr [27]. For the Ni-Co, the approximate linear dependence is observed in both studies. Regarding the Co-Cr subset, the SFEs obtained from Farkas2018 increase from Co to $Co_{0.5}Cr_{0.5}$ and decrease from $Co_{0.5}Cr_{0.5}$ to Cr, opposite to the CPA results [27]. Finally, for the concentrated compositions, the non-linear dependence of SFEs is most significant in 50% Co region ($Ni_xCo_{0.5}Cr_{0.5-x}$) using Farkas2018, contrary to the 50% Cr region ($Ni_xCo_{0.5-x}Cr_{0.5}$) using CPA [27]. Nevertheless, the results from both Farkas2018 and CPA can be explained by decomposing the non-linear effects in the ternary alloys into binary contributions. The decomposition indicates that the alloying effects on the SFEs are mostly based on pairwise interactions using both methods. It should be noted that the results using either interatomic potentials or the CPA may be reasonable in certain compositions but insufficiently accurate in other regions of the ternary diagram.

The SFEs of the two ternary alloys from Choi2018 are shown in Fig. 9. The deviations from the compositional linear mixing are relatively small using this potential and the maximum differences are 14.0 and 7.1 mJ/m^2 for Ni-Co-Cr and Ni-Co-Fe, respectively. For Ni-Co-Cr, the potential yields lower SFEs than the linear-mixing estimation for almost all considered compositions. The non-linearity comes mostly from Ni-Cr pair, followed by Co-Cr pair, and the Ni-Co edge almost has no deviation. For Ni-Co-Fe, the linear mixing serves as a fair estimation, especially near the equiatomic region. However, the non-linearity cannot be simply decomposed into pair contributions.

Numerically, the Choi2018 potential produces low SFEs for pure Cr and Fe (-152.2 mJ/m^2 and -103.6 mJ/m^2, respectively), which not only lead to low SFE in Cr/Fe-abundant region with the body-centered cubic (bcc) phase but also affect the SFEs in concentrated regions. For example, the SFE of equiatomic NiCoCr alloy is derived to be -40.9 mJ/m^2 using the Choi2018 potential, which is dramatically lower than the aforementioned experimental value (~10–30 mJ/m^2). Therefore, the probability of the deformation-induced twinning might be overestimated, and the instability of the fcc phase should be considered if we adopt Choi2018 in the related simulations of equiatomic NiCoCr alloy.

We then compare the results of Choi2018, Farkas2018, and the CPA study [27]. In Ni-Co-Cr, Choi2018 predicts that the SFE is a convex function of the alloy concentration, i.e., the linear mixing overestimates the SFEs in most of the regions, which is opposite to Farkas2018. The non-linearity is most-significant at the region of 50% Cr ($Ni_xCo_{0.5-x}Cr_{0.5}$) based on Choi2018, different from Farkas2018, but consistent with the CPA method [27]. However, this agreement with the CPA might be incidental, as Choi2018 exhibits much weaker non-linear compositional dependence than the CPA. In addition, the SFE is barely changed if tuning Co composition alone while keeping the compositions of the other two equal, i.e., $(Ni_{0.5}Cr_{0.5})_xCo_{1-x}$, according to both Choi2018 and the CPA method. This is because the SFE of Co is almost identical to the SFE of $Ni_{0.5}Cr_{0.5}$ using the Choi2018 potential, while the treatment of the magnetic states was considered to be the cause in the CPA study [27]. In both alloys, the SFEs from Choi2018 are systematically lower than those from Farkas2018, except in Ni-rich region (the top corner of the ternary plots).

3.3. Spatial characters of the SFE fluctuation

To characterize the spatial fluctuation of SFE in interatomic potential-based simulations, we first calculated the atomic fault energy (AFE, defined in Section 2.4) with Farkas2018 potential for equiatomic alloys NiCo, NiFe, NiCoCr, NiCoFe, NiCoCrFe, and NiCoCrFeCu. Their atomistic configurations are created by randomly assigning the chemical species at lattice sites and the size of CTB is ~ 30 nm × 30 nm. We choose the (1 1 1) layer that is right below the CTB and divide the layer into square regions with a characteristic length, e.g., ~ 2.5 nm × 2.5 nm. The fault energy of a region, or regional SFE as we refer below, is derived as the average AFE of the atoms belonging to that region. We take the difference between regional SFEs at certain characteristic length and the regional SFE of the whole (1 1 1) layer for NiFe and plot them in Fig. 10 (a) – (c). We find the fluctuations of regional SFEs gradually reduce when the characteristic length increases. We further compare the standard deviation of SFEs at 2.5 nm of several equiatomic alloys (Fig. 10d) and find that the fluctuation generally increases with the chemical complexity of the materials. For instance, the fluctuation roughly increases with the number of elements in the alloys, but the binary NiFe shows stronger fluctuation than ternary NiCoFe and quaternary NiCoCrFe stronger than NiCoCrFeCu, demonstrating the importance of the chemical character of the constituted elements. Fe is the element that

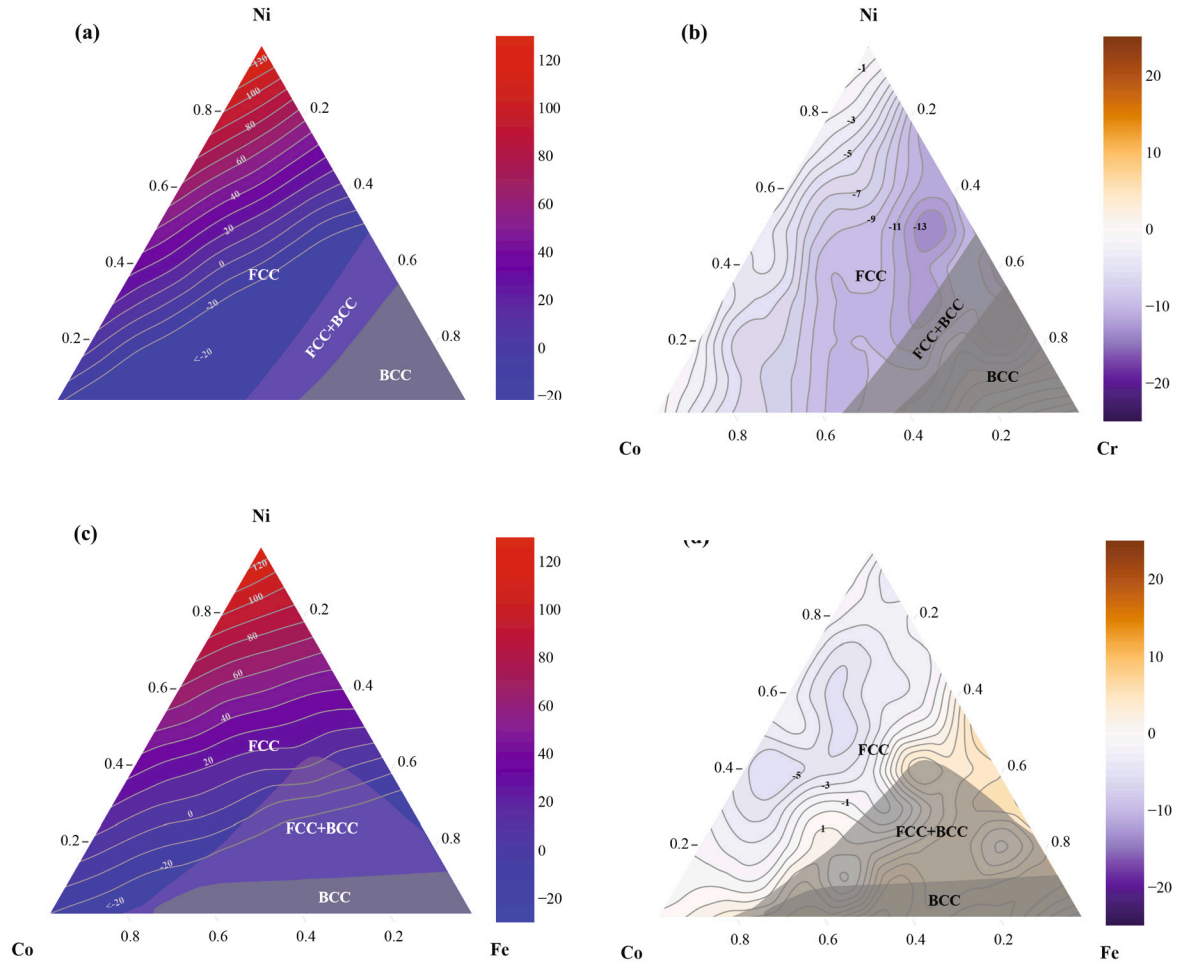

Fig. 9. Choi2018 results of (a). The SFEs of Ni-Co-Cr ternary alloys, (b). Their differences from the linear-mixing estimation, (c). The SFEs of Fe-Ni-Co alloys, and (d). Their differences from the linear-mixing estimation. The contour lines are rendered in gray. The unit of the color bars is mJ/m^2.

increases the fluctuation the most, followed by Cr. In comparison, the addition of Co or Cu in the presence of Fe reduces the fluctuation slightly.

The above simulations demonstrate that the fluctuation of the SFEs is an intrinsic feature of these alloys. In fact, the fluctuations of SFEs discussed in Section 3.1.4 is not a statistical issue caused by the limited supercell size in DFT. Rather, it is a ubiquitous phenomenon in solid-solution alloys as a consequence of their intrinsic randomness, particularly prominent at concentrated compositions. Such spatial fluctuations of SFE/GSFE alone can be a source of strengthening as indicated by a dislocation dynamic simulations [19] and a stochastic extension of the Peierls-Nabarro model [20]. The former study assumes regions of uniform SFEs whose sizes and the magnitude of inter-regional SFE fluctuation serve as inputs for dislocation dynamic simulations. According to this model, both region size and magnitude of the fluctuation contribute to the strengthening of materials.

The fluctuations of regional SFEs observed in our simulations indicate that a region with a uniform SFE does not physically exist without the presence of short-range ordering (SRO) or local chemical ordering (LCO) and should be considered as an approximation. The presence of SRO may further influence the fluctuations by forming regions of distinct chemical compositions. For example, in NiCoCr, Co, and Cr tend to segregate and form Co-Cr-rich regions at low temperatures while the regions are interconnected by Ni [30]. In such a system with potentially a segregation, the SRO may reduce the fluctuations of SFEs within a given region and increases the difference of SFEs between the regions. Additionally, the fluctuations for these systems are determined by the size of the segregates and are different from the scenarios in randomly distributed alloys. Further investigations are needed to fully examine the influences of SRO on the fluctuations of mechanical properties in the concentrated alloys.

4. Summary

In this study, the stacking fault energies (and twining energies) of Ni-based concentrated alloys are determined using both DFT and atomistic simulations. For Ni-Cu, Ni-Co, and Ni-Fe alloys, different dependences of SFEs on the alloy composition are found using DFT. Ni-Co essentially follows the linear-mixing rule. Ni-Cu exhibits a transition of dependence related to the magnetic phase transition. Ni-Fe possesses an overall convex trend as a function of composition, which is considered to be caused by the magnetic effects of the alloys. Moreover, we systematically evaluated the available EAM and MEAM potentials of the examined alloys and consider that Choi2018 and Farkas2018 provide the overall highest fidelity.

Using the interatomic potentials with the overall highest fidelity, the SFE calculations are extended to ternary Ni-Co-Cr and Ni-Co-Fe alloys. The Farkas2018 potential dramatically overestimate the SFEs of Ni-Co-Cr near the equiatomic concentration compared to the experimental results while Choi2018 significantly underestimate the values. The non-linear compositional effects in Ni-Co-Cr can be decomposed into binary interactions using Farkas2018 and CPA method [27] but are generally more complex in the ternary alloys. These results provide a basis to evaluate the limitations of using these potentials for simulations of SFE-

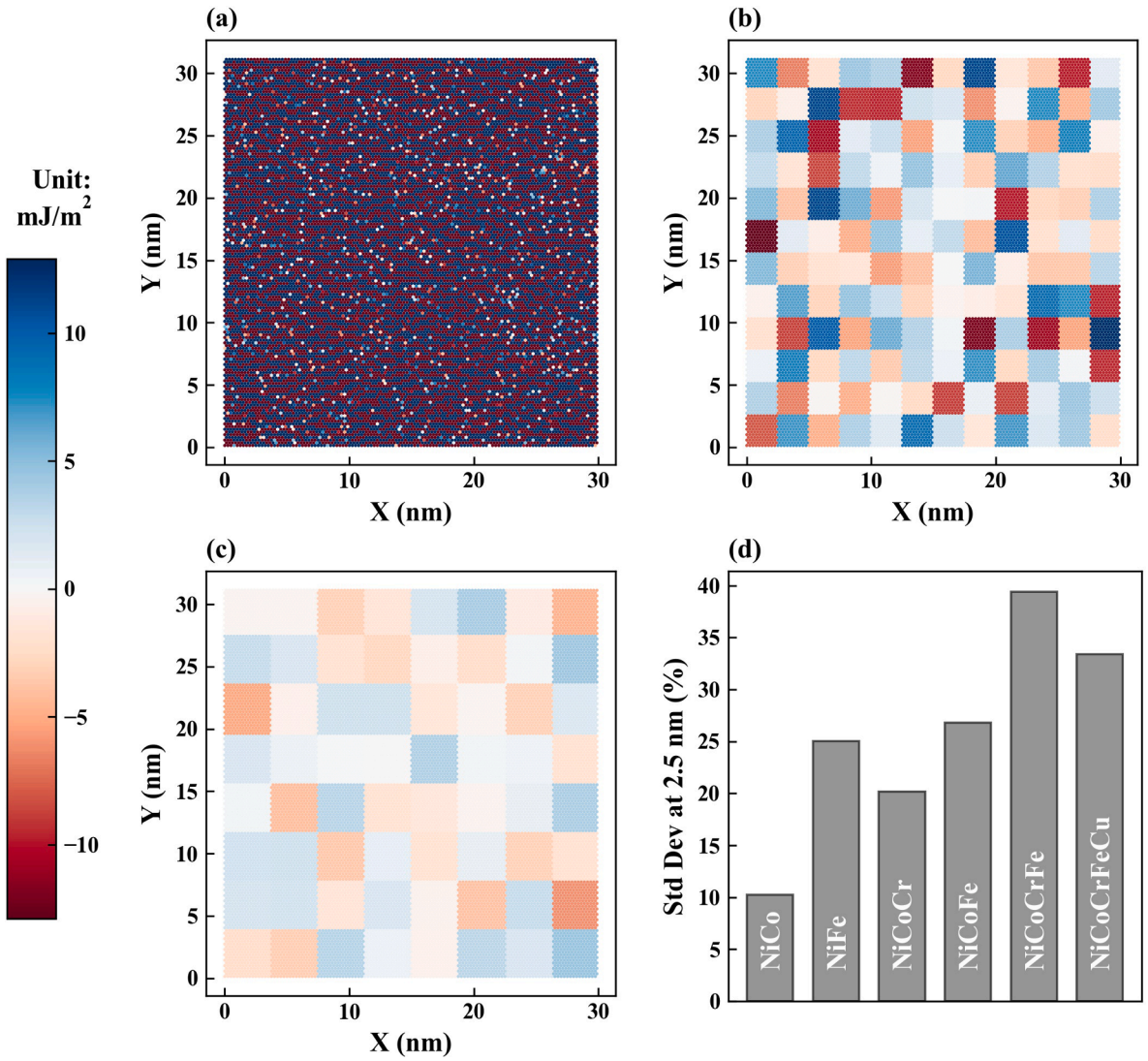

Fig. 10. (a), (b), and (c) Spatial distribution of the fault energies of Ni-Fe at the characteristic length of around 1.25, 2.5, and 3.75 nm, respectively; (d) standard deviation of the regional fault energies at 2.5 nm in some fcc equiatomic alloys obtained using the Farkas2018 potential.

related properties, such as the separation distance of Shockley partials, and deformation processes.

The statistical fluctuation of SFEs and its compositional dependence is quantified in the binary alloys at DFT level. The magnitude of the fluctuation seems to correlate qualitatively with the configurational entropy of the alloys, particularly in Ni-Cu and Ni-Co. The fluctuation has been revealed to be influenced by the characters, e.g., magnetic structure, of the constituent elements. Meanwhile, the spatial fluctuations of SFEs of the concentrated alloys are found to be substantial at nanometer scale in the atomistic simulations. The fluctuation of SFEs rising from the randomness of atomistic and magnetic/electronic configurations is an intrinsic feature of the concentrated alloys, influencing the physical properties of these alloys.

This study provides a fundamental understanding of the compositional effects on the SFEs and twinning energies, which could serve as the basis for further investigations of the deformation mechanisms in the Cantor and Cantor-like alloys. More broadly, this study focuses on mechanical properties in compositional regions beyond the dilute-limit, a much larger space in the phase diagram, which could allow a systematic tuning of mechanical properties in non-equimolar alloys for the future design of advanced alloys.

CRediT authorship contribution statement

Liubin Xu: Investigation, Methodology, Data curation, Formal analysis, Writing - original draft, Visualization. **Luis Casillas-Trujillo:** Data curation, Formal analysis, Writing - review & editing. **Yanfei Gao:** Formal analysis, Writing - review & editing, Supervision. **Haixuan Xu:** Conceptualization, Methodology, Formal analysis, Writing - review & editing, Supervision, Project administration, Funding acquisition.

Declaration of Competing Interest

The authors declare that they have no known competing financial interests or personal relationships that could have appeared to influence the work reported in this paper.

Acknowledgments

L. X. and H. X. are supported by the National Science Foundation under Grant No. DMR-1654438. Y. G. acknowledges the support of the National Science Foundation under Grant No. DMR-1809640. This work used the Extreme Science and Engineering Discovery Environment (XSEDE), which is supported by the National Science Foundation grant number TG-DMR170112.

Data availability

The raw/processed data required to reproduce these findings cannot be shared at this time due to technical or time limitations. However, those data are available from the corresponding author(s) upon reasonable request.

References

[1] J.-W. Yeh, S.-K. Chen, S.-J. Lin, J.-Y. Gan, T.-S. Chin, T.-T. Shun, C.-H. Tsau, S.-Y. Chang, Nanostructured high-entropy alloys with multiple principal elements: novel alloy design concepts and outcomes, Adv. Eng. Mater. 6 (5) (2004) 299–303.
[2] B. Cantor, F. Audebert, M. Galano, K. Kim, I. Stone, P.J. Warren, Novel multicomponent alloys, J. Metastable Nanocrystalline Mater., Trans Tech Publ (2005) 1–6.
[3] K.K. Alaneme, M.O. Bodunrin, S.R. Oke, Processing, alloy composition and phase transition effect on the mechanical and corrosion properties of high entropy alloys: a review, J. Mater. Res. Technol. 5 (4) (2016) 384–393.
[4] D.B. Miracle, O.N. Senkov, A critical review of high entropy alloys and related concepts, Acta Mater. 122 (2017) 448–511.
[5] J. Chen, X.Y. Zhou, W.L. Wang, B. Liu, Y.K. Lv, W. Yang, D.P. Xu, Y. Liu, A review on fundamental of high entropy alloys with promising high-temperature properties, J. Alloy. Compd. 760 (2018) 15–30.
[6] W.D. Li, P.K. Liaw, Y.F. Gao, Fracture resistance of high entropy alloys: a review, Intermetallics 99 (2018) 69–83.
[7] Z.Y. Lyu, X.S. Fan, C. Lee, S.Y. Wang, R. Feng, P.K. Liaw, Fundamental understanding of mechanical behavior of high-entropy alloys at low temperatures: a review, J. Mater. Res. 33 (19) (2018) 2998–3010.
[8] E.P. George, D. Raabe, R.O. Ritchie, High-entropy alloys, Nat. Rev. Mater. 4 (8) (2019) 515–534.
[9] E.P. George, W.A. Curtin, C.C. Tasan, High entropy alloys: A focused review of mechanical properties and deformation mechanisms, Acta Materialia (In Press, Available online Dec 2019).
[10] F. Otto, A. Dlouhy, C. Somsen, H. Bei, G. Eggeler, E.P. George, The influences of temperature and microstructure on the tensile properties of a CoCrFeMnNi high-entropy alloy, Acta Mater. 61 (15) (2013) 5743–5755.
[11] Z. Wu, H. Bei, G.M. Pharr, E.P. George, Temperature dependence of the mechanical properties of equiatomic solid solution alloys with face-centered cubic crystal structures, Acta Mater. 81 (2014) 428–441.
[12] Z.H. Jin, P. Gumbsch, E. Ma, K. Albe, K. Lu, H. Hahn, H. Gleiter, The interaction mechanism of screw dislocations with coherent twin boundaries in different face-centred cubic metals, Scr. Mater. 54 (6) (2006) 1163–1168.
[13] J.Y. Zhang, H.W. Zhang, H.F. Ye, Y.G. Zheng, Twin Boundaries merely as Intrinsically Kinematic Barriers for Screw Dislocation Motion in FCC Metals, Sci Rep-Uk 6 (2016).
[14] A. Gali, E.P. George, Tensile properties of high- and medium-entropy alloys, Intermetallics 39 (2013) 74–78.
[15] N.L. Okamoto, S. Fujimoto, Y. Kambara, M. Kawamura, Z.M.T. Chen, H. Matsunoshita, K. Tanaka, H. Inui, E.P. George, Size effect, critical resolved shear stress, stacking fault energy, and solid solution strengthening in the CrMnFeCoNi high-entropy alloy, Sci. Rep.-Uk 6 (2016).
[16] G. Laplanche, A. Kostka, C. Reinhart, J. Hunfeld, G. Eggeler, E.P. George, Reasons for the superior mechanical properties of medium-entropy CrCoNi compared to high-entropy CrMnFeCoNi, Acta Mater. 128 (2017) 292–303.
[17] S.F. Liu, Y. Wu, H.T. Wang, J.Y. He, J.B. Liu, C.X. Chen, X.J. Liu, H. Wang, Z.P. Lu, Stacking fault energy of face-centered-cubic high entropy alloys, Intermetallics 93 (2018) 269–273.
[18] A.J. Zaddach, C. Niu, C.C. Koch, D.L. Irving, Mechanical Properties and stacking fault energies of NiFeCrCoMn high-entropy alloy, Jom-Us 65 (12) (2013) 1780–1789.
[19] Y. Zeng, X. Cai, M. Koslowski, Effects of the stacking fault energy fluctuations on the strengthening of alloys, Acta Mater. 164 (2019) 1–11.
[20] L.C. Zhang, Y. Xiang, J. Han, D.J. Srolovitz, The effect of randomness on the strength of high-entropy alloys, Acta Mater. 166 (2019) 424–434.
[21] S. Huang, W. Li, S. Lu, F.Y. Tian, J. Shen, E. Holmstrom, L. Vitos, Temperature dependent stacking fault energy of FeCrCoNiMn high entropy alloy, Scr. Mater. 108 (2015) 44–47.
[22] S.J. Zhao, G.M. Stocks, Y.W. Zhang, Stacking fault energies of face-centered cubic concentrated solid solution alloys, Acta Mater. 134 (2017) 334–345.
[23] C. Niu, C.R. LaRosa, J. Miao, M.J. Mills, M. Ghazisaeidi, Magnetically-driven phase transformation strengthening in high entropy alloys, Nat. Commun. 9 (1) (2018) 1363.
[24] P.J. Yu, Y. Zhuang, J.P. Chou, J. Wei, Y.C. Lo, A. Hu, The influence of dilute aluminum and molybdenum on stacking fault and twin formation in FeNiCoCr-based high entropy alloys based on density functional theory, Sci. Rep.-Uk 9 (2019).
[25] C. Slone, C.R. LaRosa, C. Zenk, E.P. George, M. Ghazisaeidi, M.J. Mills, Deactivating deformation twinning in medium-entropy CrCoNi with small additions of aluminum and titanium, Scr. Mater. 178 (2020) 295–300.
[26] Y. Ikeda, I. Tanaka, J. Neugebauer, F. Körmann, Impact of interstitial C on phase stability and stacking-fault energy of the CrMnFeCoNi high-entropy alloy, Phys Rev Mater 3 (11) (2019), 113603.
[27] Y. Ikeda, F. Körmann, I. Tanaka, J. Neugebauer, Impact of chemical fluctuations on stacking fault energies of CrCoNi and CrMnFeCoNi high entropy alloys from first principles, Entropy 20 (9) (2018) 655.
[28] S.J. Zhao, Y. Osetsky, G.M. Stocks, Y.W. Zhang, Local-environment dependence of stacking fault energies in concentrated solid-solution alloys, npj Comput. Mater. 5 (2019).
[29] J. Ding, Q. Yu, M. Asta, R.O. Ritchie, Tunable stacking fault energies by tailoring local chemical order in CrCoNi medium-entropy alloys, Proc. Natl. Acad. Sci. 115 (36) (2018) 8919–8924.
[30] Q.-J. Li, H. Sheng, E. Ma, Strengthening in multi-principal element alloys with local-chemical-order roughened dislocation pathways, Nat. Commun. 10 (1) (2019) 3563.
[31] X. Wu, Z. Li, Z. Rao, Y. Ikeda, B. Dutta, F. Körmann, J. Neugebauer, D. Raabe, Role of magnetic ordering for the design of quinary TWIP-TRIP high entropy alloys, Phys. Rev. Mater. 4 (3) (2020), 033601.
[32] R. Zhang, S. Zhao, J. Ding, Y. Chong, T. Jia, C. Ophus, M. Asta, R.O. Ritchie, A. M. Minor, Short-range order and its impact on the CrCoNi medium-entropy alloy, Nature 581 (7808) (2020) 283–287.
[33] W.-M. Choi, Y.H. Jo, S.S. Sohn, S. Lee, B.-J. Lee, Understanding the physical metallurgy of the CoCrFeMnNi high-entropy alloy: an atomistic simulation study, npj Comput. Mater. 4 (1) (2018) 1.
[34] D. Farkas, A. Caro, Model interatomic potentials and lattice strain in a high-entropy alloy, J. Mater. Res. 33 (19) (2018) 3218–3225.
[35] S. Kibey, J.B. Liu, D.D. Johnson, H. Sehitoglu, Predicting twinning stress in fcc metals: linking twin-energy pathways to twin nucleation, Acta Mater. 55 (20) (2007) 6843–6851.
[36] Y. Su, S. Xu, I.J. Beyerlein, Density functional theory calculations of generalized stacking fault energy surfaces for eight face-centered cubic transition metals, J. Appl. Phys. 126 (10) (2019), 105112.
[37] G. Kresse, J. Hafner, Ab initio molecular dynamics for liquid metals, Phys. Rev. B 47 (1) (1993) 558.
[38] G. Kresse, J. Furthmüller, Efficiency of ab-initio total energy calculations for metals and semiconductors using a plane-wave basis set, Comput. Mater. Sci. 6 (1) (1996) 15–50.
[39] J.P. Perdew, K. Burke, M. Ernzerhof, Generalized gradient approximation made simple, Phys. Rev. Lett. 77 (18) (1996) 3865.
[40] M. Methfessel, A. Paxton, High-precision sampling for Brillouin-zone integration in metals, Phys. Rev. B 40 (6) (1989) 3616.
[41] J. Kudrnovský, V. Drchal, P. Bruno, Magnetic properties of fcc Ni-based transition metal alloys, Phys. Rev. B 77 (22) (2008).
[42] H.P. Wijn, Magnetic Properties of Metals: d-Elements, Alloys and Compounds, Springer Science & Business Media, 2012.
[43] A. Zunger, S.H. Wei, L.G. Ferreira, J.E. Bernard, Special quasirandom structures, Phys. Rev. Lett. 65 (3) (1990) 353–356.
[44] A. Van De Walle, M. Asta, G. Ceder, The alloy theoretic automated toolkit: a user guide, Calphad 26 (4) (2002) 539–553.
[45] A. Van de Walle, P. Tiwary, M. De Jong, D. Olmsted, M. Asta, A. Dick, D. Shin, Y. Wang, L.-Q. Chen, Z.-K. Liu, Efficient stochastic generation of special quasirandom structures, Calphad 42 (2013) 13–18.
[46] H.J. Monkhorst, J.D. Pack, Special points for Brillouin-zone integrations, Phys. Rev. B 13 (12) (1976) 5188–5192.
[47] NIST Interatomic Potentials Repository (https://www.ctcms.nist.gov/potentials/).
[48] G. Bonny, R.C. Pasianot, N. Castin, L. Malerba, Ternary Fe–Cu–Ni many-body potential to model reactor pressure vessel steels: First validation by simulated thermal annealing, Phil. Mag. 89 (34–36) (2009) 3531–3546.
[49] B. Onat, S. Durukanoglu, An optimized interatomic potential for Cu-Ni alloys with the embedded-atom method, J Phys-Condens Mat 26 (3) (2014).
[50] G.P. Purja Pun, V. Yamakov, Y. Mishin, Interatomic potential for the ternary Ni–Al–Co system and application to atomistic modeling of the B2–L10 martensitic transformation, Modell. Simula. Mater. Sci. Eng. 23 (6) (2015).
[51] G. Bonny, D. Terentyev, R.C. Pasianot, S. Poncé, A. Bakaev, Interatomic potential to study plasticity in stainless steels: the FeNiCr model alloy, Modell. Simul. Mater. Sci. Eng. 19 (8) (2011).
[52] G. Bonny, N. Castin, D. Terentyev, Interatomic potential for studying ageing under irradiation in stainless steels: the FeNiCr model alloy, Modell. Simul. Mater. Sci. Eng. 21 (8) (2013).
[53] X.W. Zhou, M.E. Foster, R.B. Sills, An Fe-Ni-Cr embedded atom method potential for austenitic and ferritic systems, J. Comput. Chem. 39 (29) (2018) 2420–2431.
[54] S. Plimpton, Fast parallel algorithms for short-range molecular-dynamics, J. Comput. Phys. 117 (1) (1995) 1–19.
[55] P. Denteneer, W. Van Haeringen, Stacking-fault energies in semiconductors from first-principles calculations, J. Phys. C: Solid State Phys. 20 (32) (1987) L883.
[56] H. Natter, M. Schmelzer, R. Hempelmann, Nanocrystalline nickel and nickel-copper alloys: synthesis, characterization, and thermal stability, J. Mater. Res. 13 (05) (1997) 1186–1197.
[57] A. Taylor, Lattice parameters of binary nickel cobalt alloys, J. Inst. Met. 77 (6) (1950) 585–594.
[58] M. Hayase, M. Shiga, Y. Nakamura, Spontaneous volume magnetostriction and lattice-constant of face-centered cubic Fe-Ni and Ni-Cu Alloys, J. Phys. Soc. Jpn. 34 (4) (1973) 925–931.
[59] L. Vegard, Die Konstitution der mischkristalle und die raumfüllung der atome, Zeitschrift für Physik 5 (1) (1921) 17–26.
[60] R. Weiss, The origin of theInvar'effect, Proc. Phys. Soc. 82 (2) (1963) 281.
[61] M. van Schilfgaarde, I. Abrikosov, B. Johansson, Origin of the Invar effect in iron–nickel alloys, Nature 400 (6739) (1999) 46–49.

[62] P. Marcus, V. Moruzzi, Equilibrium properties of the cubic phases of cobalt, Solid State Commun. 55 (11) (1985) 971–975.
[63] V. Moruzzi, P. Marcus, K. Schwarz, P. Mohn, Ferromagnetic phases of bcc and fcc Fe Co, and Ni, Physical Review B 34 (3) (1986) 1784.
[64] L.Y. Tian, R. Lizarraga, H. Larsson, E. Holmstrom, L. Vitos, A first principles study of the stacking fault energies for fcc Co-based binary alloys, Acta Mater. 136 (2017) 215–223.
[65] J. Chen, Y. Liu, G. Sheng, F. Lei, Z. Kang, Atomic mobilities, interdiffusivities and their related diffusional behaviors in fcc Co–Cr–Ni alloys, J. Alloy. Compd. 621 (2015) 428–433.
[66] Y.K. Yoo, Q. Xue, Y.S. Chu, S. Xu, U. Hangen, H.-C. Lee, W. Stein, X.-D. Xiang, Identification of amorphous phases in the Fe–Ni–Co ternary alloy system using continuous phase diagram material chips, Intermetallics 14 (3) (2006) 241–247.